Impingement and Mixing Dynamics of Micro-Droplets on a Solid Surface

Guina Yi [a,b], Ziqi Cai [a,b,*], Zhengming Gao[a,b,*], J.J. Derksen [c]

[a] Beijing Advanced Innovation Center for Soft Matter Science and Engineering, Beijing University of Chemical Technology, Beijing 100029, China

[b] State Key Laboratory of Chemical Resource Engineering, School of Chemical Engineering, Beijing University of Chemical Technology, Beijing 100029, China

[c] School of Engineering, University of Aberdeen, Aberdeen AB24 3UE, UK

Abstract:

The hydrodynamics and mixing during the nonaxisymmetry impingement of a micro-droplet and a sessile droplet of the same fluid are investigated by many-body dissipative particle dynamics (MDPD) simulation. In this work, the range of the impingement angle (θ_i) between the impinging droplet and the sessile droplet is 0° - 60° and the contact angle is set as 45° or 124°. The droplets impingement and mixing behavior is analyzed based on the droplet internal flow field, the concentration distribution and the time scale of the decay of the kinetic energy of the impinging droplet. The dimensionless total mixing time τ_m is calculated by a modified *mixing* function. With the Weber number(*We*) ranging from 5.65 to 22.7 and the Ohnesorge number(*Oh*) ranging from 0.136 to 0.214, we find τ_m hardly changes with *We* and *Oh*. Whereas, θ_i and surface wettability are found to have a significant effect on τ_m. We find that θ_i has no clear effect on τ_m on a hydrophobic surface, while on the hydrophilic surface, τ_m increase with the θ_i. Thus, reducing the impinging angle is a valid method to shorten the total mixing time.

Keywords: droplets impingement, mixing behavior, mixing time, concentration distribution, many-body dissipative particle dynamics.

Highlights

- Impingement on sessile micro-droplet with different impinging angles was simulated
- Convective time, diffusion time and total mixing time were determined quantitatively
- Influence factors on the dimensionless droplet mixing time were discussed
- Mixing time can be shortened by reducing the impinging angle

Supported from National Natural Science Foundation of China (No.22078008) and the Fundamental Research Funds for the Central Universities (XK1802-1).

* Corresponding author. Tel: +86-10-6441-9171; Fax: +86-10-6444-9862. E-mail address: caiziqi@mail.buct.edu.cn (Ziqi Cai) , gaozm@mail.buct.edu.cn (Zhengming Gao).

1. Introduction

Droplets impinging on solid surfaces is common in industrial and technological processes, such as electro-spraying[1] , inkjet printing[2, 3], drug delivery[4], and self-cleaning[5]. Generally, there are three types of impingement and mixing of two droplets on a solid surface, dependent on their relative position when approaching the surface, see Figure1. (a) The two droplets impinge on the surface simultaneously; (b) the successive droplets impinge on the surface; (c) the first droplet is in a sessile and equilibrated state on the surface and is hit by the second incoming drop. Here, we review the literature associated with the last, “long spacing” scenario (Figure 1c).

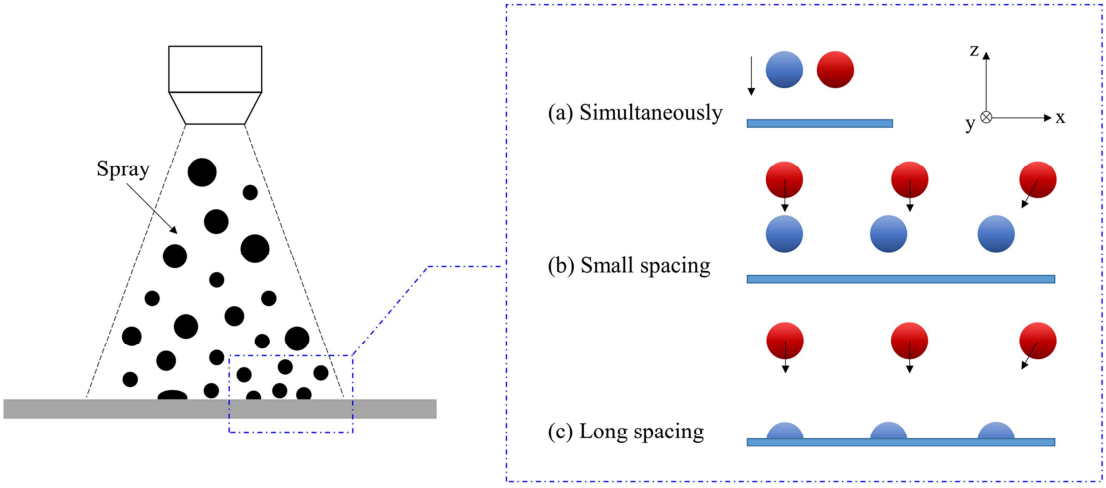

Figure 1 Schematic representation of spatial distributions of two droplets impact on a surface.

When the spacing is large enough, the leading droplet can be regarded as stationary (sessile) when the impinging droplet collides with it. In this case, the impinging droplet could rebound or coalesce after collision. During the coalescence process, there are generally three stages, namely film drainage[6], film rupture and bridge growth[7]. The coalescence process of two droplets has been investigated in many previous works [8, 9], especially for cases in which droplets are moving slowly relative to one another

When we talk about impingement or collision, the relative motion between droplets cannot be ignored. In the case of a head-on collision (the left side scenario of Figure 1c), Fujimoto et al.[10] observed a circular liquid crown after droplets collision, which was on account of a large pressure gradient near the free surface. Wakefield et al.[11] pointed that the energy dissipation contributed to the crown formation. They also found that half of the kinetic energy of the impacting droplet was dissipated when approaching to the maximum

spreading diameter. Besides droplet velocity, the relative size of two droplets[12, 13] and surface wettability[14] has also been found to affect the droplets impingement dynamics.

As for offset collision (Figure 1c – the middle scenario), the effect of the lateral offset extent between the impinging and sessile droplets on producing a stable line has been experimentally investigated by Soltman et al.[15] and Stringer et al.[16]. Duineveld et al.[17] and Ku et al.[18] studied the influence of surface property on line printing. Based on their work, the receding contact angle was a key parameter to affect the retracting behaviors of the contact line. Lee et al.[19] experimentally found that droplets with low viscosity resulted in disconnection which was undesired in line printing. An empirical correlations was proposed by Li et al.[20] to predict the spread lengths of ethylene glycol droplets. Sarojini et al.[2] studied impingement of PEDOT:PSS droplets. This is a non-Newtonian liquid used for inkjet printing. They proposed a semi-analytical expression to predict the droplet spreading for offset collision in ink jetting.

During the impingement, the time scales and levels of liquid mixing in the merged droplet on the surface have been studied experimentally and computationally by a number of researchers. Castrejón-Pita et al.[13] studied the mixing behavior between glycerol and water droplets by coloration method. They pointed that the presence of solid surface hindered the mixing. However, the mixing could be improved by stretching and folding the droplets, which could be easily achieved by setting baffles[21] or applying long serpentine channels [22, 23] in microchannel device. For 'open-surface' droplet-based microfluidics, a wettability gradient surface[24-26] is a common way to promote the droplet mixing. Recently, Sykes et al.[27] found that the mixing could be improved by the formation of an internal jet. The influence of substrate wettability, the volume ratio and droplet viscosity on the formation of the jet were studied by means of experiments and numerical simulations. Besides passive method, active method applying external force such as magnetic[28], electric[29], acoustic[30] and thermocapillary[31] force can also be used to enhance the mixing efficiency.

For a better understanding of the mixing performance of coalescing droplets on a surface, micro-PIV[32] and micro-LIF[33] techniques are widely applied for droplets of millimeter size. Micro-PIV is an efficient method to track the internal flow of the merged droplets and micro-LIF can be used to visualize the mixing patterns. Based on micro-LIF, the evolution of a mixing process can be quantified by calculating the mixing index M_i, where M_i is related to the concentration of fluorescent tracer.[26].

For small length scales, simulation is an efficient way to study the free droplet mixing behavior. Through molecular dynamics (MD) simulations, Pak et al.[34] studied the mixing of water nanodroplets in three dimensions. In their study, the *mixing* function $m(\tau)$ along one Cartesian coordinate direction x was calculated as follows:

$$m_{x,a}(\tau) = \left\langle x(\tau)^2 \right\rangle_a \Big/ \left\langle x(\tau)^2 \right\rangle_{all} \tag{1}$$

In Eq.(1), $\left\langle x(\tau)^2 \right\rangle_a$ is the average squared x coordinate of the water molecules in region a, where region a represents interfacial (I) or bulk (B) and *all* represents all molecules in the merged droplets. Analogous definitions of $m(\tau)$ is applied to the y and z coordinates. The mixing is completed when the value of $m(\tau)$ in three coordinates stabilizes at 1. This method is suitable for particle-based simulation.

From the literature reviewed above, we see that the mixing dynamics between the droplets plays an important role in the droplets pattern and the control of product quality. Most of the numerical works performed so far focus on the vertical impingement. Studies of an impinging droplet colliding with a sessile droplet under an angle are limited. In the practical application, the droplet generally has a tangential or lateral speed, especially in the spraying process. Recently, a convenient method to administer sprayable drugs for post-surgical cancer treatment was reported[35]. In this method, the fibrinogen solution and thrombin solution were sprayed in the form of microdroplets onto the tumour surface respectively. This mixture formed a gel which helped in inhibiting the local tumour recurrence and the development of distant tumours. However, after being sprayed, it cannot employ external forces to enhance the mixing between droplets. Therefore, it's necessary to realize how the mixing time of a free droplet impingement on a sessile droplet under various impinging angles was affected, which is the focus of the present work.

In this study, the three-dimensional many-body dissipative particle dynamics (MDPD) simulation was conducted to investigate the effect of impinging angle on droplets impingement and mixing behavior on surfaces with different wettability. Inertial effects and droplet properties such as droplet velocity, surface tension and viscosity were considered. These effects were quantified in terms of Weber number (*We*) and Ohnesorge number (*Oh*). All the simulations in this work were programmed in a modified MDPD code based on the LAMMPS[36] framework.

The rest of this paper is organized as follows: the numerical method and parameters applied in this study are given in Section 2. The results and discussion are described in Section 3, where we firstly study the droplets impingement behavior through snapshots, time series of contact points and the velocity field plots. Then the mixing performance is analyzed by mixing time, including the duration of convective stage, the duration of diffusive stage and the total mixing time. Thirdly, the influence of impingement angle, surface wettability, *We* and *Oh* on the total mixing time is studied. Finally, conclusions are provided in Section 4.

2.Numerical method

2.1 MDPD method

The MDPD method is a modification of the original dissipative particle dynamics (DPD) method with the purpose of simulating the coexistence of vapor and liquid[37-39]. Examples include fluid flow in nanoporous shales[40], droplets on solid surfaces[41] and gas bubble dynamics[42]. In MDPD, particles interact via forces. The interaction force $\mathbf{F_{ij}}$ between particle *i* and particle *j* has three contributions: $\mathbf{F_{ij}} = \mathbf{F_{ij}^C} + \mathbf{F_{ij}^D} + \mathbf{F_{ij}^R}$ [38].

The dissipative force $\mathbf{F_{ij}^D}$ and random force $\mathbf{F_{ij}^R}$ are the same as in the standard DPD method[43]. They are expressed as

$$\mathbf{F_{ij}^D} = -\gamma w_D(r_{ij})(\mathbf{e_{ij}} \cdot \mathbf{v_{ij}})\mathbf{e_{ij}} \tag{2}$$

$$\mathbf{F_{ij}^R} = \delta w_R(r_{ij})\xi_{ij}\Delta t^{-1/2}\mathbf{e_{ij}} \tag{3}$$

Where γ is the friction coefficient, δ is the noise amplitude; ξ_{ij} is a random Gaussian number with zero mean and unit variance; $\mathbf{v_{ij}}=\mathbf{v_i}-\mathbf{v_j}$, $r_{ij} = |\mathbf{r_{ij}}| = \mathbf{r_i}-\mathbf{r_j}$ stand for the relative velocity and distance between two particles *i* and *j*, respectively; $\mathbf{e_{ij}} = \mathbf{r_{ij}} / |\mathbf{r_{ij}}|$ denotes the unit vector from particle *j* to particle *i*. A common choice for the weight function $w_R(r_{ij})$ is $w_R(r_{ij}) = 1 - r_{ij}/r_C$. The fluctuation-dissipation theorem is satisfied when $\delta^2=2\gamma k_B T$ and $w_D(r_{ij})=[w_R(r_{ij})]^2$, where k_B is the Boltzmann's constant and *T* is the system temperature[43]. $\triangle t$ is the time step.

The conservative force $\mathbf{F_{ij}^C}$ is defined as

$$\mathbf{F_{ij}^C} = [A_{ij} w_C(r_{ij}) + B_{ij}(\bar{\rho}_i + \bar{\rho}_j) w_d(r_{ij})]\mathbf{e_{ij}} \tag{4}$$

Where $A_{ij}w_C(r_{ij})$ represents the long-range attractive part and $B_{ij}(\bar{\rho}_i+\bar{\rho}_j)w_d(r_{ij})$ represents the short-range repulsive part. Generally, $A_{ij}>0$ and $B_{ij}<0$. The weight function $w_C(r_{ij}) = 1 - r_{ij}/r_C$ and $w_d(r_{ij}) = 1 - r_{ij}/r_d$ with the cutoff range r_c and r_d.

The local density ρ at the location of particle i can be obtained by $\bar{\rho}_i = \sum_{j\neq i} w_\rho(r_{ij})$ where $w_\rho(r_{ij}) = \frac{15}{2\pi r_d^3}\left(1-\frac{r_{ij}}{r_d}\right)^2$, [38,44].

2.2 Simulation setup

The schematic representation of our simulation system is depicted in Figure 2 with two droplets of the same liquid. In the present study, the interaction parameters between liquid particles are the same as in our pervious report[45], which was on the interaction of droplet with patterned surfaces, i.e. $A_{ij} = -40$, $B_{ij} = 25$, r_c=1.0, and r_d = 0.75. For this set of parameters, the density and the surface tension of the liquid are determined to be ρ=6.09 and σ=7.51 based on individual simulations following the methods according to [45, 46] . The scaling coefficients between the physical and MDPD units are $L_{MDPD} = 1.32 \times 10^{-6}$ m, $M_{MDPD} = 4.01 \times 10^{-16}$ kg, and $T_{MDPD} = 2.31 \times 10^{-7}$ s according to our pervious report[45]. The substrate is made of frozen particles randomly placed and the density of substrate is the same as that of the liquid. The bounce-forward[47] boundary condition is applied. The impinging droplet of radius R_C =14 consists of 69849 MDPD particles and the sessile droplet has the same volume, density ρ, surface tension σ and dynamic viscosity μ as the impinging droplet.

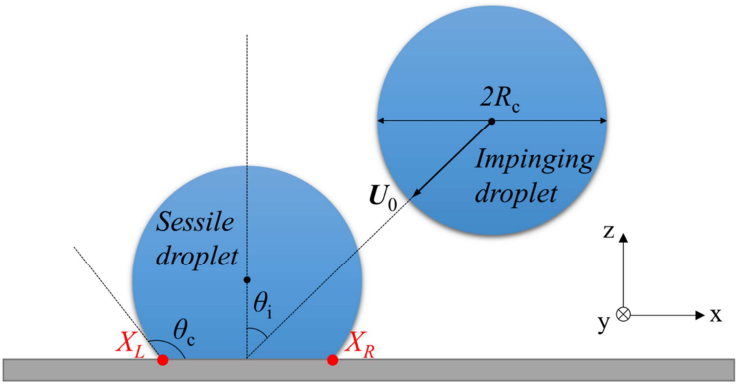

Figure 2 Schematic of an impinging droplet impact on a sessile droplet having contact angle θ_c at an impingement angle θ_i.

In this simulation, the Bond number $Bo=\frac{\rho g R_c^2}{\sigma}$ (g the gravitational acceleration) is much smaller than 10^{-3} so that the effect of gravity is neglected. A standard velocity-Verlet algorithm is used for the simulation and the time step is set to $\triangle t$=0.01 in MDPD unit[45].

The simulations are performed in a three-dimensional computational domain of size 150 × 100 × 70, with periodic boundary condition in the *x* and *y* direction with the coordinate system defined in Figure 2. First, the sessile droplet is obtained by releasing a spherical droplet to the substrate without velocity. By changing the long-range attractive part coefficient A_{sl} between the liquid particles and the solid particles, we can obtain the substrate wettability as expected. After the droplet reaches an equilibrium state with a static contact angle θ_c, the impinging droplet, with a velocity of U_0 and a certain impingement angle θ_i, is loaded into the calculation box. The angle between vertical line and the line connecting the center of the impinging droplet and the center of the footprint of the sessile droplet is set as θ_i. as shown in Figure 2. Time is normalized as $\tau = t\sigma/(\mu R_c)$, where t is the MDPD time. In order to make sure that the beginning moment of the collision process is the same for each run, the minimum distance between the surfaces of two types of particles is set to $1r_c$, and the simulation is initialized under this condition. More settings detail is shown in Table1. It should be noted that *Oh* is varied with the liquid viscosity, and the liquid viscosity can be obtained by changing the friction coefficient γ. Micron droplets were chosen to lie within the operating parameters found in inkjet printing[13] and general medical spray[48]. In a typical inkjet printing system, for example, the droplet velocity is 5m/s and droplet viscosity is 10mPa s[13]. In this work, the droplet velocity is 3-6m/s and droplet viscosity is 6 - 10 mPa s. Thus, the range of *We* here is from 5.68 to 22.7, and the range of *Oh* here is from 0.136 to 0.214.

Table 1. Parameters settings in MDPD simulations

Description	MDPD units	Physical units
Radius, R_c	14	18.5 μm
density, ρ	6.09	1056 kg/m^3
Surface tension, σ	7.51	56.5 mN/m
dynamic viscosity, μ	4.872 (γ=1)	0.0064 Pas
	7.649 (γ=18)	0.01 Pas
static contact angle, θ_c	45° (A_{sl}=37),124° (A_{sl}=20)	
impinging angle θ_i.	0°, 30°, 45°, 60°	
Weber number, $We=\frac{2\rho U_0^2 R_c}{\sigma}$	5.68, 22.7	
Ohnesorge number, $Oh=\frac{\mu}{\sqrt{2\rho R_c \sigma}}$	0.136, 0.214	

3.Results and discussion

3.1 Droplet impingement behavior

In this section, we focus on the impingement behavior of a droplet colliding with a sessile droplet under different impingement angles. The Weber number of the impinging droplet has been fixed to 22.7 and the Ohnesorge number to 0.136. The wetting properties of the substrate are set as hydrophilic (θ_c=45°) or hydrophobic (θ_c=124°).

Impressions of the impingement process under the various conditions are shown in Figure 3. The momentum exchange between the liquid in the two coalescing drops gives rise to a moving three-phase contact line. This has been quantified in Figure 4 that shows time series of the outer left and right points on the contact line as well as of the center of the drop's footprint on the surface. Strong droplet deformations are observed for $\tau \leq 20$. During later period, deformations are much less. The hydrophobic merged drop, however, keeps sliding in the negative *x*-direction over the surface until $\tau \approx 100$ for non-zero impingement angles as a result of the negative *x*-momentum of the incoming droplet (see Figure 4). The sliding distances for hydrophilic droplet are at least one order of magnitude less than the hydrophobic droplet due to the much stronger adhesion on the substrate. The head-on and small-angle collisions of the hydrophobic droplets give rise to oscillations of the three-phase contact line with a temporary retraction which is strongest at $\tau \approx 20$.

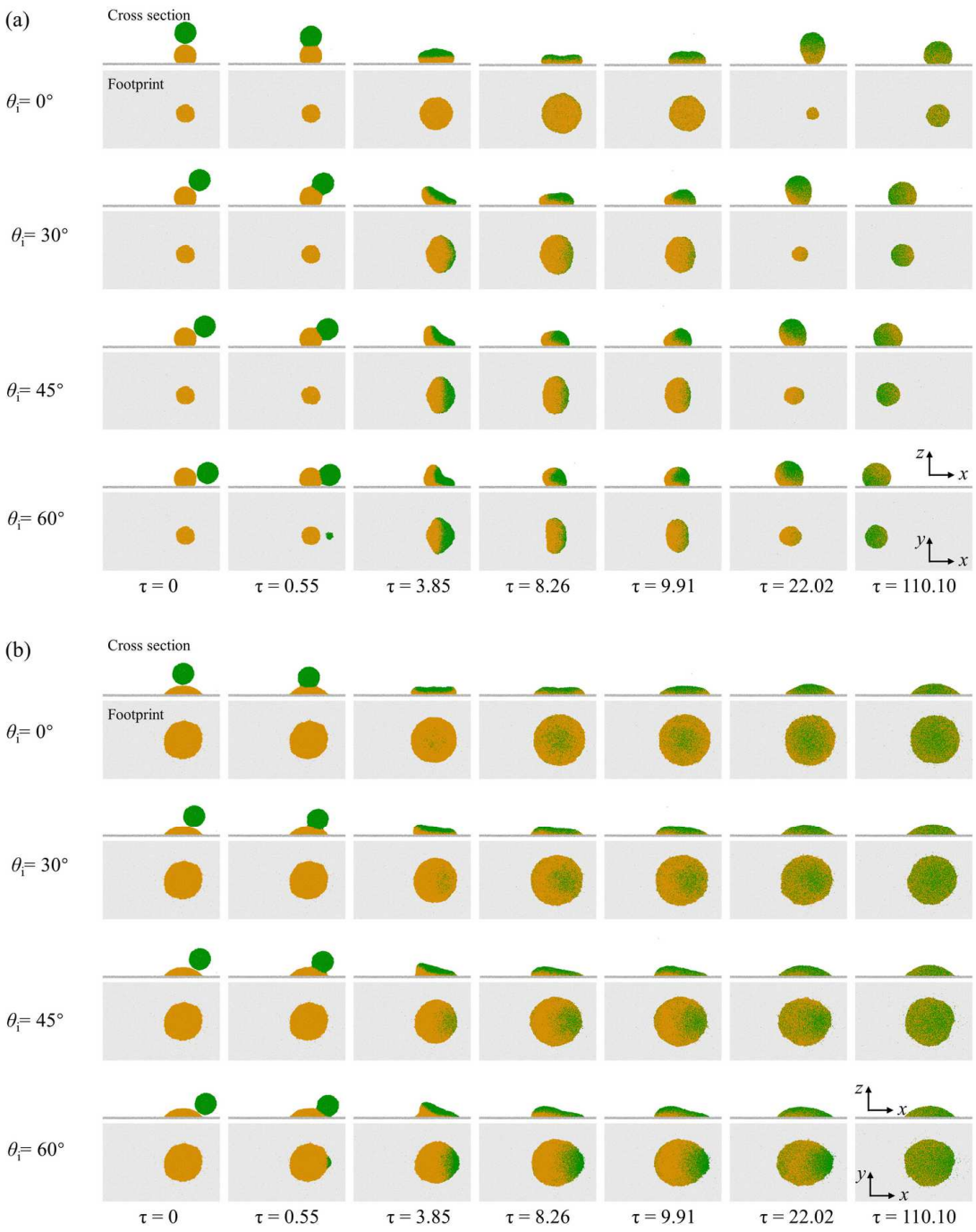

Figure 3 Snapshots of droplet (green) impingement on a sessile droplet (amber) at various impingement angles θ_i on (a) hydrophobic surface and on (b) hydrophilic surface.

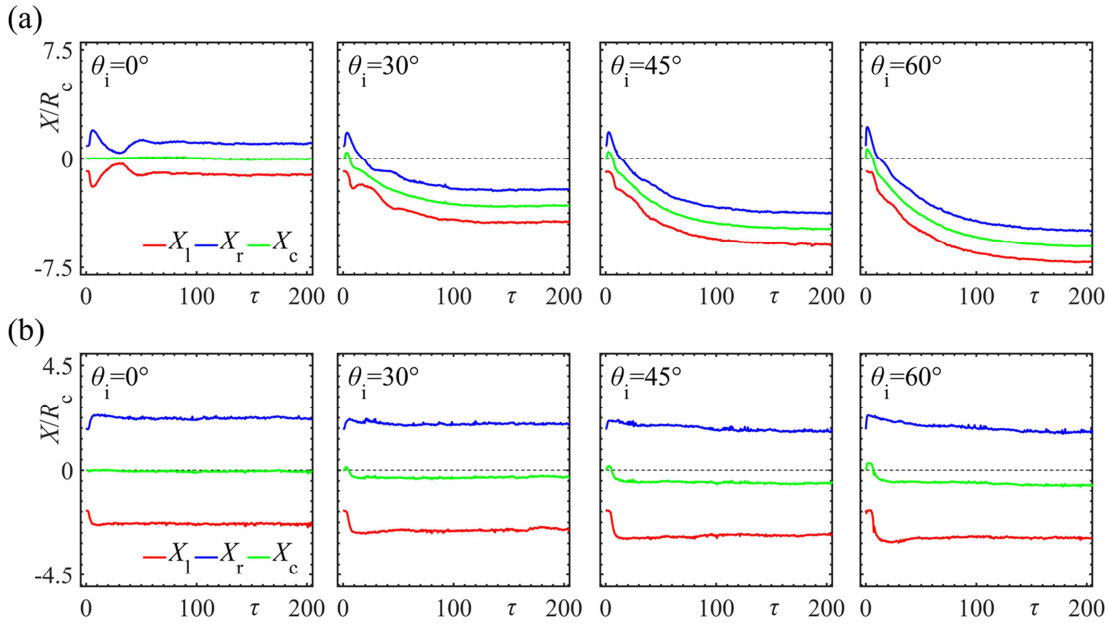

Figure 4. Time series of contact points (as defined in Figure 2) displacement of merged droplet on (a) hydrophobic surface and (b)hydrophilic surface. $x_c = (x_r + x_l)/2$

Further insight on the flow dynamics inside the droplet has been obtained by visualizing its velocity field, as done in Figure 5. For this we need the ensemble-average. If we take a single realization, the velocity field is overwhelmed by random thermal motion of the molecules (as in Figure 5a). For this reason, we repeat the impingement process 50 times, each with a different, statistically independent initial randomization. The result of the velocity field is shown in Figure 5b. If we subtract the average velocity of the droplet we arrive at Figure 5c that shows that the impingement generates an internal recirculation in the hydrophobic droplet at $\tau \approx 14$. In Lai et al [24] experiment, they also found an internal recirculation pattern based on a micro-LIF measurement.

The velocity fields in the hydrophilic droplet (Figures 5e and f) show a recirculation at short times ($\tau \approx 5$) but not anymore at $\tau \approx 14$. Apparently the stronger adhesion and smaller wall normal length scales of the hydrophilic droplet dissipate internal flow much faster as compared to the hydrophobic droplet.

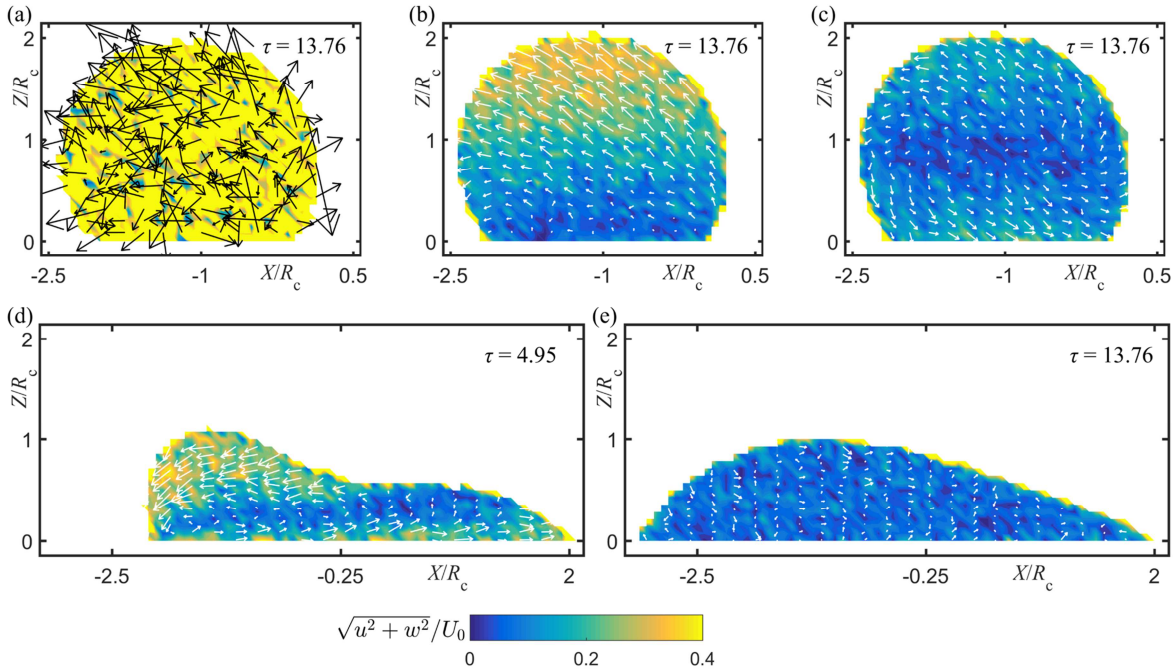

Figure 5 (a-c) Velocity fields inside merged droplets on hydrophobic surface. (a) Single realization. (b) Ensemble averaged realization. (c) Ensemble averaged velocity field relative to the average velocity of droplet $\vec{\mathbf{v}}$ ($\vec{\mathbf{v}} = \frac{1}{N}\sum_{i=1}^{N}\vec{\mathbf{v}}_i$, N the particle number in merged droplets). (d) and (e) ensemble averaged velocity field relative to the average velocity inside the merged droplet on a hydrophilic surface. The impingement angle(θ_i) equals 45°.

3.2 Droplet mixing performance

The mixing of two miscible droplets is achieved through convective mass transfer (organized motion of molecules) and diffusive mass transfer (random motion of molecules). A common method to estimate the mixing performance experimentally in the stage of diffusive mass transfer is the mixing index (see Eq. 1). Three-dimensional experimental evaluation of the convective stage is limited due to the limitation of sampling rate and concentration distribution reconstruction efficiency after a complete 3D scan[24]. However, this drawback can be overcome in a simulation.

3.2.1 Droplet kinetic energy

First the mixing performance in the stage of convective mass transfer is evaluated by tracking the kinetic energy of the impinging droplet. The variation of scaled kinetic energy E_k^*, together with the variation of the velocity of the impinging droplet in three directions is shown in Figure 6. Here, the kinetic energy of the impinging droplet E_k is calculated as

$$\vec{v}_{mean}=\frac{1}{N}\sum_{i=1}^{N}\vec{v}_i$$
$$E_k=\frac{1}{2}M|\vec{v}_{mean}|^2=\frac{1}{2}M(v_{x,mean}^2+v_{y,mean}^2+v_{z,mean}^2) \quad (5)$$

Where, N is the number of particles in the impinging droplet. And the scaled kinetic energy is defined as $E_k^*=E_k/E_k^0$, where E_k^0 is the initial kinetic energy of the impinging droplet with the velocity unity.

As shown in the Figure 6, E_k^* shows a fluctuation when it generally decreases in the cases of droplets on hydrophobic surface at θ_i=0° and θ_i=30°. Mehran et al.[49] also found the fluctuation of kinetic energy when a droplet impact on a sessile droplet with an offset distance. They calculated the variation of energy and pointed that kinetic and surface energy were interchanging between each other and viscous dissipation occurs during the impingement. In this work, when the kinetic energy increases during the fluctuation, it generally results in the velocity component normal to the surface. However, due to the adhesion between droplet and surface, the merged droplet cannot detach from the surface, thus E_k^* stabilizes at zero finally.

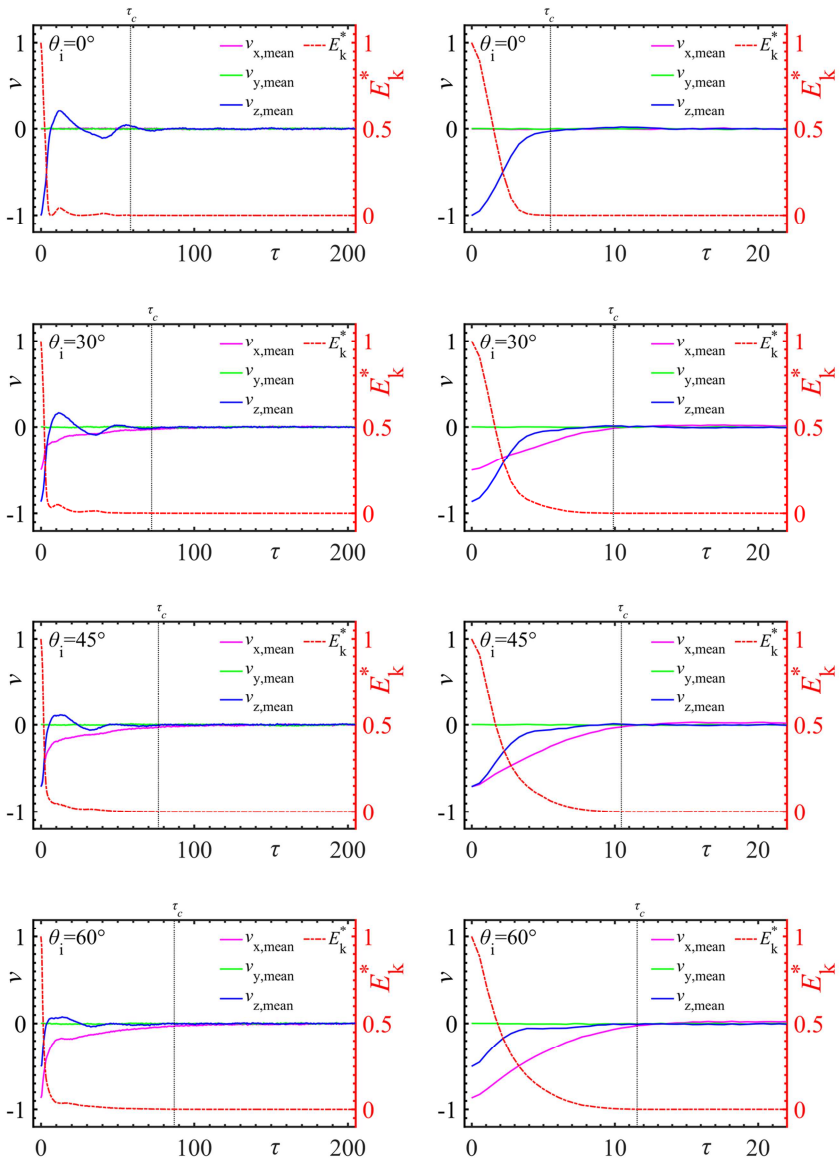

Figure 6 The mean velocity $\vec{v}_{mean}$ and the scaled kinetic energy E_k^* of the impinging droplet as a function of time. τ_c indicate the when the $E_k^* < 0.001$. Left hydrophobic, right hydrophilic. *We*= 22.7, *Oh*=0.136.

We assume that the convective mixing stage is finished when the kinetic energy of the impinging droplet is low enough, such as $E_k^* < 10^{-3}$. We find that the value of τ_c in the case of hydrophobic surface are all larger than that in the case of hydrophilic surface. This is because the attraction between hydrophilic surface and liquid particles is larger than that between hydrophobic surface and liquid particles, and this attraction hinders convection in the droplet. Additionally, the value of τ_c increases with θ_i. This is because of the increase of initial velocity in the horizontal direction v_x, and the increased time required for the droplet to come to rest under the same surface condition.

The variation of droplet velocities can also indicate that there is diffusion of droplet particles. When collision happens, the particles in the impinging droplet move towards the sessile droplet as the velocities of impinging droplet decreases. The particle motion in y direction cannot be illuminated in Figure 6, since the collision is symmetric about the *x*-*z* plane, which results in the value of the mean velocity in y direction remains zero all the time.

3.2.2 Droplet internal concentration field

Figure 7 shows the mixing inside the merging droplets in terms of concentration contours of the liquid in the sessile droplet. The method to extract concentration distribution is shown in Figure 8. Firstly, a slice with the thickness of 1 on the *x*-*z* plane ($y \in$ [-0.5, 0.5]) is extracted from the merged droplet (Figure 8a), and then this slice is divided into cubes with a side length of 1 (Figure 8b). By counting the number of particles belonging to the impinging and sessile droplet respectively, the concentration of the liquid originally belonging to the sessile droplet in this cube can be calculated. Finally, the instantaneous concentration field in the merged droplet can be obtained by averaging 50 cases with different random seeds. Here, the local mixing is illustrated by the variation of concentration of sessile droplet, C_1; a value of 0.5 implies a full mixing, whereas C_1=0 or C_1=1 indicates complete segregation.

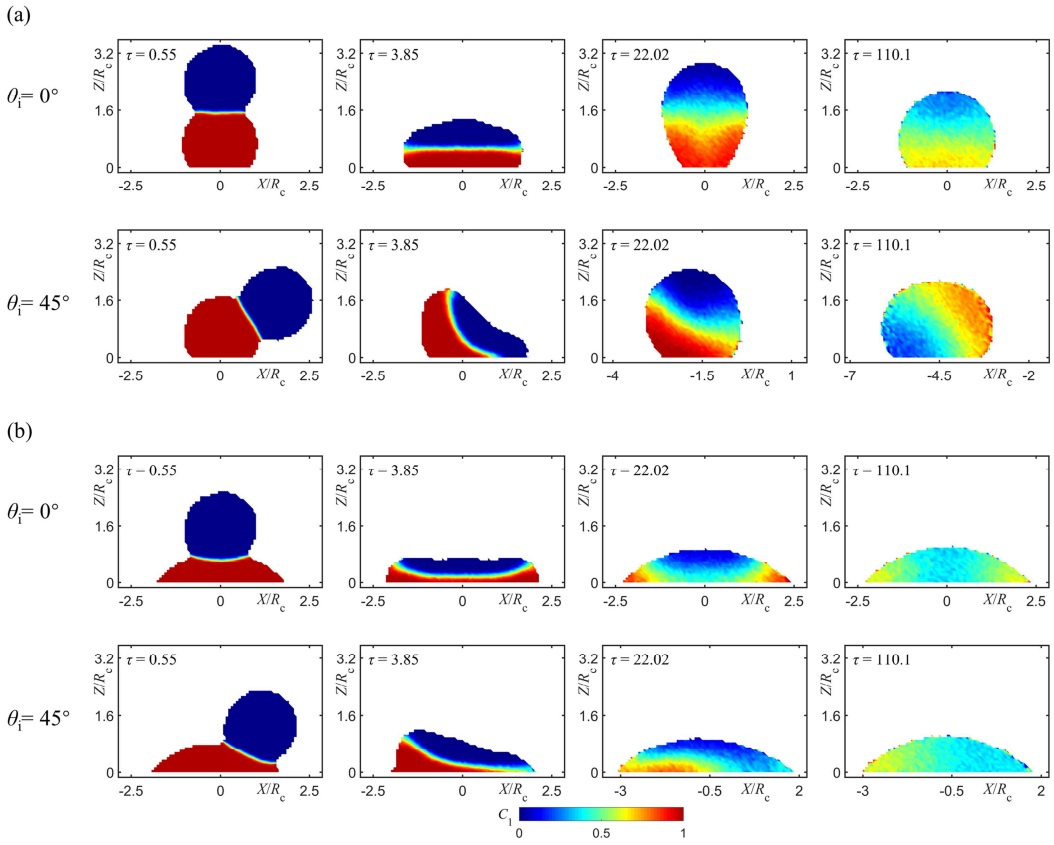

Figure 7 The instantaneous concentration of *sessile droplet* on (a) hydrophobic surface and (b) hydrophilic surface. *We* = 22.7, *Oh* = 0.136

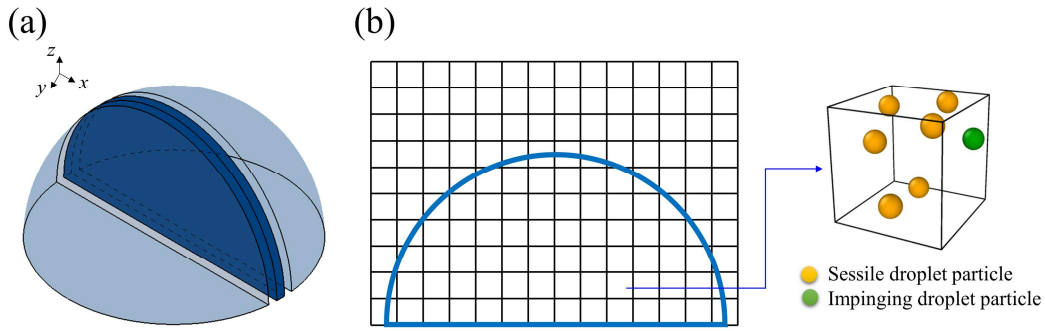

Figure 8 Schematic diagram of calculation method of concentration profile field in a cross section of the merged drop.

At the beginning of droplets contact, the interface is well-defined (τ = 0.55). After some time (τ = 3.85-110.1), the interface becomes indistinct and the mixed area ($C_1 \approx 0.5$) increases around the interface as a result of diffusion. This phenomenon can be observed under various conditions, see Figure 7. For head-on collision, the mixed area appears in the middle for hydrophobic surface with the liquid particles diffusing upwards and downwards; whereas for hydrophilic surface the liquid particles diffuse radially. For the asymmetric collision, the mixed area also is asymmetric, where the leading part of sessile droplet and trailing part of impinging droplet are still unmixed (τ = 22.02). In addition, we can see that the concentration gradient direction in the merged hydrophobic droplet is reversed between the moments τ = 22.02 and τ =

110.1 when θ_i is 45°, which is because that the merged droplet is "rolling up" on the hydrophobic surface and the impinging droplet gradually becomes a part of the leading edge (Figure 3a θ_i=45°, τ = 22.02 -110.1). From Figure 7, we also can find that the droplet is still not fully mixed when the convective mixing stage is over.

3.2.3 Total mixing time

The total mixing time of two droplets are indicated by the *mixing functions* proposed by Pak et al.[34], based on the distribution of liquid molecules in three-dimensional space:

$$\begin{aligned} m_{\mathrm{x},a}(\tau) &= \left\langle x(\tau)^2 \right\rangle_a \Big/ \left\langle x(\tau)^2 \right\rangle_{all} \\ m_{\mathrm{y},a}(\tau) &= \left\langle y(\tau)^2 \right\rangle_a \Big/ \left\langle y(\tau)^2 \right\rangle_{all} \\ m_{\mathrm{z},a}(\tau) &= \left\langle z(\tau)^2 \right\rangle_a \Big/ \left\langle z(\tau)^2 \right\rangle_{all} \end{aligned} \tag{6}$$

Here, a is the sessile droplet part(S) or impinging droplet part(I), and "all" represents the merged droplet part. By calculating the average of the square of particle coordinates ($\langle x(\tau)^2 \rangle$, $\langle y(\tau)^2 \rangle$, and $\langle z(\tau)^2 \rangle$) in three dimensions, the particles can be regarded as completely mixed when the $m_{x,a}(\tau)$=$m_{y,a}(\tau)$ = $m_{z,a}(\tau)$ =1. When calculating the value of $m(\tau)$, we take the center of the footprint of the sessile droplet as the origin of the coordinate system.

The variation of $m(\tau)$ with time is plotted in Figure 9. For head-on collision, the change of $m_x(\tau)$ and $m_y(\tau)$ with time are the same, indicating – as expected – the same mixing rate in both x and y direction. For $\theta_i > 0$ cases, the values of $m_x(\tau)$ and $m_z(\tau)$ decline rapidly (τ = 0 to τ = 10) due to the quick movement of the particles from impinging droplet to sessile droplet as soon as the collision begins.

Additionally, we also learn that the droplets are not fully mixed at the end of the convective stage, since the $m(\tau)$ does not stabilize at 1 after τ reaches τ_c (τ_c is shown in Figure 6). It still takes more time to reach full mixing, and after τ_c the molecular diffusion dominates the mixing process.

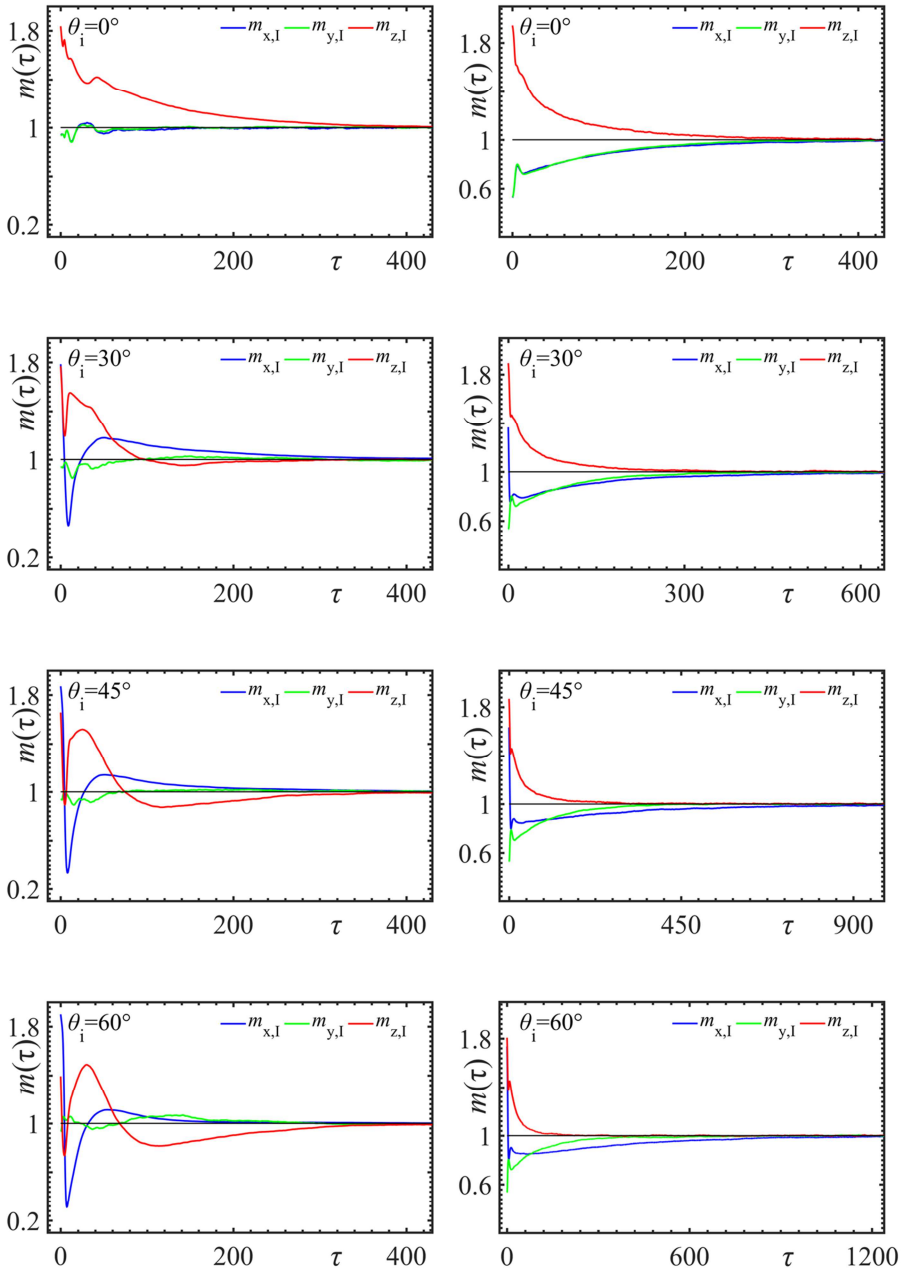

Figure 9 Mixing progress of the droplets on hydrophobic surface (left column) and hydrophilic surface (right column) expressed in terms of the m(τ) functions. *We* = 22.7, *Oh* = 0.136. Since m(τ) cannot exactly become equal to one, we obtained τ_c when $|1\text{- m}(\tau)| \leq 0.01$.

The dimensionless total mixing time of the droplet for different *We* and *Oh* combinations is plotted in Figure 10a, where *We* is varied by changing the droplet velocity U_0 (see Figure 2) and *Oh* is varied by changing the droplet viscosity μ. We can see that *We* and *Oh* hardly have an effect on τ_m. The mixing time of hydrophobic droplets is smaller than hydrophilic droplets, and the mixing time increases as θ_i increases on a hydrophilic surface.

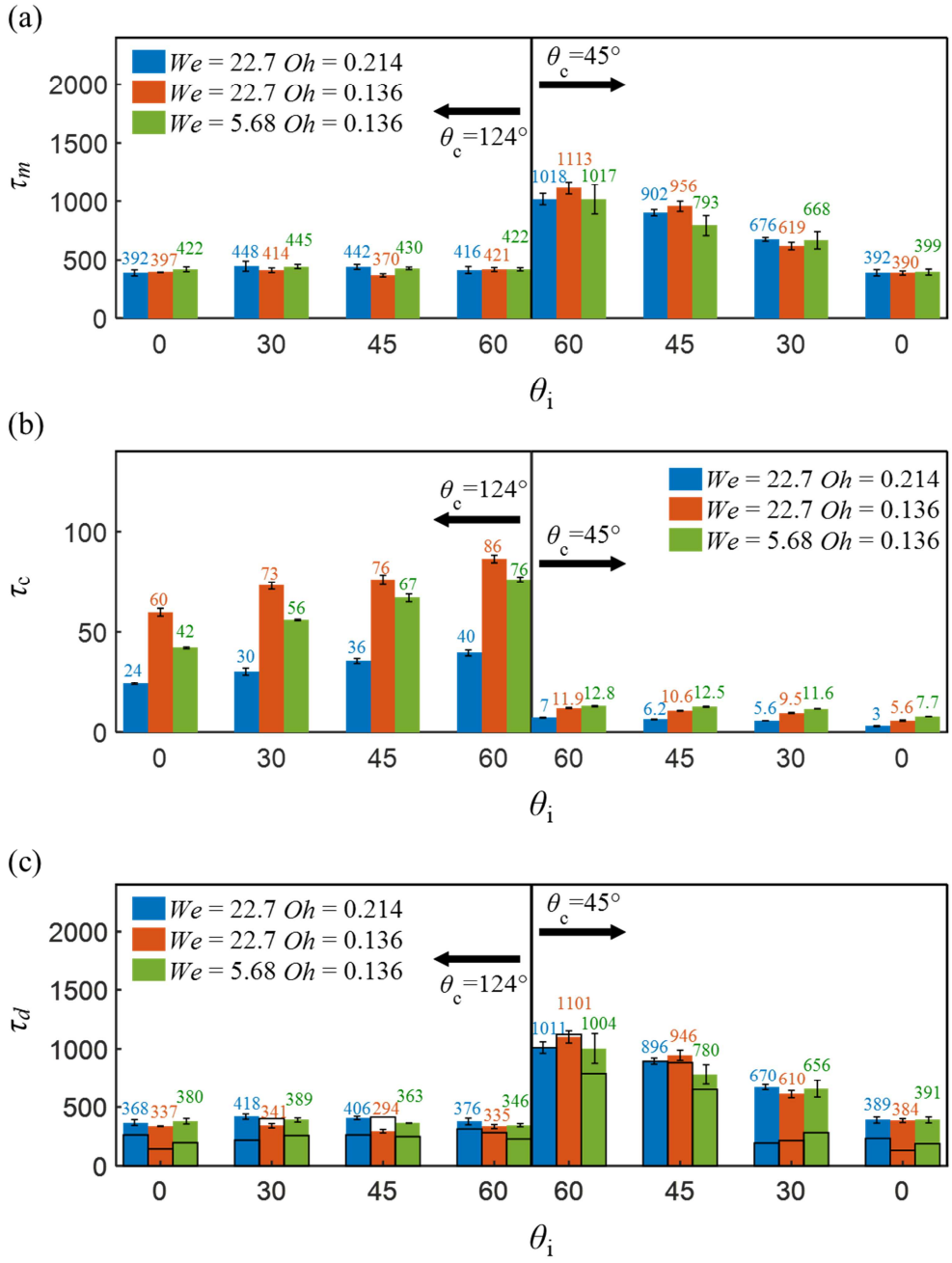

Figure 10. (a)Total mixing time, (b)flow time of the droplets under different conditions and (c)diffusion time of the droplets derived by total mixing time minus flow time. The hollow bar with black frame is the estimation value, and an error bar represents one standard deviation.

3.2.4 Convective time and diffusion time

In order to interpret the difference of τ_m under various conditions, the convective time(τ_c) and the diffusion time(τ_d) are calculated respectively. As shown in Figure 10(b) and(c), we can see that the influence of *We* and *Oh* on τ_c is not as great as that of surface wettability. Besides, larger θ_i results in a longer τ_c, indicating that the internal recirculation lasts longer and fluid disperses vertically and horizontally. It is reported that this internal recirculation can benefit mixing[24] However, in this work, we find that a longer τ_c does not lead to a shorter total mixing time. This is because in this mixing process, τ_c is one order of

magnitude smaller than τ_d, which means the total mixing time is dominated by diffusion. However, the convection eventually does determine the initial state of the diffusion process as shown in Figure 11, which then affects the total mixing time.

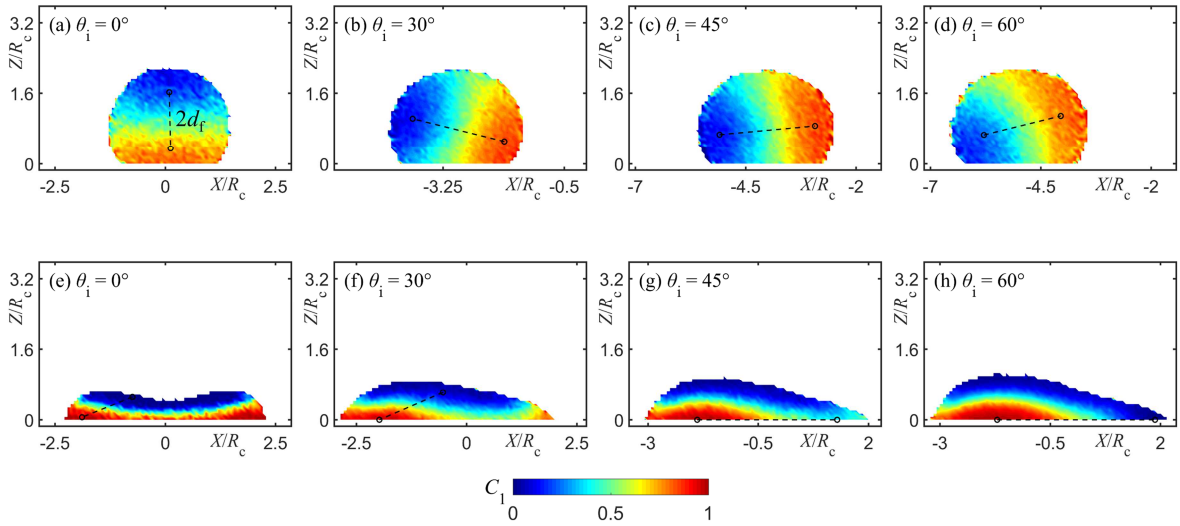

Figure 11. The determination of diffusion length on (a-d) hydrophobic surface and on (e-h) hydrophilic surface when *Oh*=0.136 *We*=22.7 after convective stage is over. A dash line represents one distance from the main high concentration location to the main low concentration location, where the main high concentration location and main low concentration location is dependent on the concentration distribution (see Figure 12). And this distance equals twice the diffusion distance d_f.

We estimates τ_d by the squared diffusion length divided by self-diffusion coefficient, where the self-diffusion coefficient(*D*) can be determined through the Einstein equation[50]:

$$\mathrm{D} = \frac{1}{6}\lim_{\mathrm{t}\to 0}\frac{\mathrm{d}}{\mathrm{dt}}\left(\mathrm{MSD(t)}\right) \tag{7}$$

where the Mean-Square-Displacement of the freely diffusing particle along the time (*MSD(t)*) can be written as

$$MSD\left(t\right) = \left\langle \left|\mathbf{r}_i\left(t\right) - \mathbf{r}_i\left(0\right)\right|^2 \right\rangle \tag{8}$$

where $\mathbf{r_i}(t) - \mathbf{r_i}(0)$ is the vector distance traveled by a given particle over the time interval. From this method, for example, for the case *Oh*=0.136, we can get the self-diffusion coefficient *D* is 0.0615; and for the case *Oh*=0.214, the diffusion coefficient *D* is 0.039.

Diffusion distance, which is related to the concentration distribution in the bulk, is another important factor determining the diffusion time. In order to determine the diffusion distance, we count the percentage of particles in the concentration range of 0 to 1.0 for each case at the end of the convection stage, seen in

Figure 12 as an example. In the figure, two concentration peaks occur at C_1=0.2 and C_1=0.85, respectively, which means most particles are in the concentration of C_1=0.2 and of C_1=0.85. Therefore, these two values can be regarded presenting the bulk concentration for the corresponding case, and the diffusion distance (d_f) is defined as half of the distance marked by dashed line pieces in the panel of Figure 11.

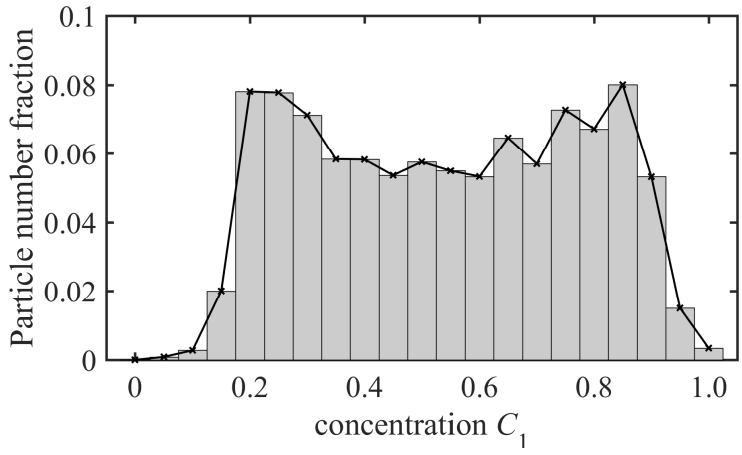

Figure 12. The particle number fraction over a range of concentrations for the case [θ_c=124° θ_i=30° *Oh*=0.136 *We*=22.7]. The concentration interval is 0.05. The largest particle number fraction occurs at C_1=0.85 if C_1>0.5 and C_1=0.2 if C_1<0.5

For the hydrophilic cases we notice that the horizontal concentration gradients largely exist in the near wall layer when $\theta_i \geq 45°$. And in these cases, when we count the percentage of particles in the concentration range, only the particles closed to the surface (within $0.5r_c$) are considered.

The estimated diffusion time are shown in Figure 10(c) in bar with black frame. Comparing with the diffusion time calculated by the total mixing time minus flow time, the trend of the diffusion time along the impinging angle has been captured. Since we consider the diffusion distance as the distance over a concentration difference of the majority of particles, a small part of particle whose diffusion distance larger than majority's has not been considered, which results in the underestimation of diffusion time in some cases.

In addition, the dimensionless Pelect number (*Pe*) is usually used to describe the competition between convection and diffusion. Herein, we obtain the droplet *Pe* at the end of the convection stage by $Pe = \frac{R_c|\vec{v}_{mean}|}{D}$ (R_c the initial radius of the impinging droplet, $\vec{v}_{mean}$ the average velocity of impinging droplet and *D* the diffusion coefficient of the liquid particles) and find that the value of *Pe* is ~O(10^0), that is to say, diffusive mass transfer becomes more important than convective mass transfer thereafter. Therefore, the

method to distinguish the convection stage and diffusion stage by the decay of the kinetic energy of the impinging droplet is valid in this work.

We can conclude that the θ_i and surface wettability affect the droplet concentration distribution at the start of the diffusion stage. And the concentration distribution then affects d_f. For hydrophobic surface, although the concentration distribution is different under different θ_i cases, d_f shows little difference. For hydrophilic surface, however, d_f increases with θ_i, and the increase d_f results in an increase τ_d. Compared to a hydrophilic droplet, a hydrophobic droplet has a smaller d_f. To sum up, the mixing time can be shortened by reducing the imping angle and applying the hydrophobic surface due to the smaller diffusion distance.

Conclusions

The impingement and mixing of one droplet impinging on a sessile droplet under an angle θ_i is a common phenomenon in spraying. In this work, it is investigated through a particle-based simulation method, many-body dissipative particle dynamics(MDPD). The focus of this work is to understand the impingement and mixing dynamics of droplets on the solid surface.

The snapshots, the temporal histories of contact edge and horizontal displacement of the merged droplet help to show droplets behavior during the impingement. We find that the merged droplets travel faster and further on hydrophobic surface than that on hydrophilic surface, and there is a larger migration displacement along with larger θ_i. By an ensemble-averaged method, it is shown that an internal recirculation inside the merged droplets is generated during the impingement.

The mixing performance can be characterized by the mixing time. The local mixing efficiency has been obtained by visualizing the concentration of sessile droplet in the merged droplet. It is found that the fully mixed area is around the collision interface and the area increases along with time as a result of diffusion,

The dimensionless total mixing time(τ_m) is determined by a modified *mixing* function. We find that *We* and the *Oh* hardly have an effect on τ_m. If the solid surface is hydrophilic, a larger θ_i results in a larger τ_m. However, on the hydrophobic surface, the τ_m is insensitive to θ_i.

To understand the determinants of τ_m, the convection time(τ_c) and the diffusion time(τ_d) are quantitatively determined respectively. We found that τ_c is much smaller than τ_d, meanwhile, based on the concentration distribution in the bulk during the convection stage, the droplet state at the end of convection determines the diffusion distance. Also, as expected, the diffusion distance of hydrophobic droplets is shorter than that of hydrophilic droplets. For hydrophobic droplets, the diffusion distance is not dependent on θ_i. For hydrophilic droplets, however, a largely horizontal concentration gradients exist in the near wall layer when $\theta_i \geq 45°$, resulting in a larger diffusion distance in those cases. Therefore, reducing the impingement angle is an effective means to shorten the mixing time for those mixing process where the active methods cannot be applied, such as choosing a proper spraying nozzle to reduce the spray angle in the application of sprayable drugs for post-surgical cancer treatment[35].

This work concentrates on the study of droplet impingement and mixing on a homogeneous solid surface. Inhomogeneous surfaces are common in nature and industrial applications, so that droplets impinging and mixing on such surfaces is worth investigating in the future.

Acknowledgement

The authors gratefully acknowledge the financial support from National Natural Science Foundation of China (No.22078008) and the Fundamental Research Funds for the Central Universities (XK1802-1).

Reference

[1] H. Hu, S. Rangou, M. Kim, P. Gopalan, V. Filiz, A. Avgeropoulos, C.O. Osuji, Continuous Equilibrated Growth of Ordered Block Copolymer Thin Films by Electrospray Deposition, ACS Nano, 7 (2013) 2960-2970.
[2] K. Sarojini Kg, P. Dhar, S. Varughese, S.K. Das, Coalescence Dynamics of PEDOT:PSS Droplets Impacting at Offset on Substrates for Inkjet Printing, Langmuir, 32 (2016) 5838-5851.
[3] M.Y. Teo, S. Kee, N. RaviChandran, L. Stuart, K.C. Aw, J. Stringer, Enabling Free-Standing 3D Hydrogel Microstructures with Microreactive Inkjet Printing, ACS Appl. Mater. Interfaces, 12 (2020) 1832-1839.
[4] Y. He, R. Foralosso, G.F. Trindade, A. Ilchev, L. Ruiz-Cantu, E.A. Clark, S. Khaled, R.J.M. Hague, C.J. Tuck, F.R.A.J. Rose, G. Mantovani, D.J. Irvine, C.J. Roberts, R.D. Wildman, A Reactive Prodrug Ink Formulation Strategy for Inkjet 3D Printing of Controlled Release Dosage Forms and Implants, Adv. Ther., 3 (2020) 1900187.
[5] Z. Jin, H. Mei, L. Pan, H. Liu, L. Cheng, Superhydrophobic Self-Cleaning Hierarchical Micro-/Nanocomposite Coating with High Corrosion Resistance and Durability, ACS Sustainable Chem. Eng., (2021) 4111-4121.
[6] D.Y.C. Chan, E. Klaseboer, R. Manica, Film drainage and coalescence between deformable drops and bubbles, Soft Matter, 7 (2011) 2235-2264.
[7] D.G.A.L. Aarts, H.N.W. Lekkerkerker, Droplet coalescence: drainage, film rupture and neck growth in ultralow interfacial tension systems, Int. J. Fluid Mech. Res., 606 (2008) 275-294.

[8] J.D. Paulsen, J.C. Burton, S.R. Nagel, Viscous to Inertial Crossover in Liquid Drop Coalescence, Phys Rev Lett, 106 (2011) 114501.
[9] S. Perumanath, M. Borg, M. Chubynsky, J. Sprittles, J. Reese, S. D, Droplet Coalescence is Initiated by Thermal Motion, Phys Rev Lett, 122 (2019) 104501.1-104501.6.
[10] H. Fujimoto, Collision of a droplet with a hemispherical static droplet on a solid, Int. J. Multiphase Flow, 27(2001) 1227-1245.
[11] J. Wakefield, C.F. Tilger, M.A. Oehlschlaeger, The interaction of falling and sessile drops on a hydrophobic surface, Exp. Therm. Fluid Sci., 79 (2016) 36-43.
[12] M. Kumar, R. Bhardwaj, K.C. Sahu, Coalescence dynamics of a droplet on a sessile droplet, Phys. Fluids, 32 (2020) 012104.
[13] J.R. Castrejón-Pita, K.J. Kubiak, A.A. Castrejón-Pita, M.C.T. Wilson, I.M. Hutchings, Mixing and internal dynamics of droplets impacting and coalescing on a solid surface, Phys. Rev. E, 88 (2013) 1-11.
[14] P.J. Graham, M.M. Farhangi, A. Dolatabadi, Dynamics of droplet coalescence in response to increasing hydrophobicity, Phys. Fluids, 24 (2012) 112105.
[15] D. Soltman, V. Subramanian, Inkjet-Printed Line Morphologies and Temperature Control of the Coffee Ring Effect, Langmuir, 24 (2008) 2224-2231.
[16] J. Stringer, B. Derby, Formation and Stability of Lines Produced by Inkjet Printing, Langmuir, 26 (2010) 10365-10372.
[17] Duineveld, C. P., The stability of ink-jet printed lines of liquid with zero receding contact angle on a homogeneous substrate, J. Fluid Mech., 477 (2003) 175-200.
[18] X. Cheng, Y. Zhu, L. Zhang, D. Zhang, T. Ku, Lattice Boltzmann simulation of droplets coalescence in a film patterning process on nonideal surfaces, Computers & Fluids, 176 (2018) 68-78.
[19] M.W. Lee, N.Y. Kim, S. Chandra, S.S. Yoon, Coalescence of sessile droplets of varying viscosities for line printing, Int. J. Multiphase Flow, 56 (2013) 138-148.
[20] R. Li, N. Ashgriz, S. Chandra, J.R. Andrews, S. Drappel, Coalescence of two droplets impacting a solid surface, Exp. Fluids, 48 (2010) 1025-1035.
[21] Y. Fu, H. Wang, X. Zhang, L. Bai, Y. Jin, Y. Cheng, Numerical simulation of liquid mixing inside soft droplets with periodic deformation by a lattice Boltzmann method, J. Taiwan Inst. Chem. Eng., 98 (2019) 37-44.
[22] M. Guo, X. Hu, F. Yang, S. Jiao, Y. Wang, H. Zhao, G. Luo, H. Yu, Mixing Performance and Application of a Three-Dimensional Serpentine Microchannel Reactor with a Periodic Vortex-Inducing Structure, Ind. Eng. Chem. Res., 58 (2019) 13357-13365.
[23] E. Ghazimirsaeed, M. Madadelahi, M. Dizani, A. Shamloo, Secondary Flows, Mixing, and Chemical Reaction Analysis of Droplet-Based Flow inside Serpentine Microchannels with Different Cross Sections, Langmuir, 37 (2021) 5118-5130.
[24] Y.-H. Lai, M.-H. Hsu, J.-T. Yang, Enhanced mixing of droplets during coalescence on a surface with a wettability gradient, Lab on a Chip, 10 (2010) 3149-3156.
[25] S.-I. Yeh, H.-J. Sheen, J.-T. Yang, Chemical reaction and mixing inside a coalesced droplet after a head-on collision, Microfluid. Nanofluid., 18 (2015) 1355-1363.
[26] S.-I. Yeh, W.-F. Fang, H.-J. Sheen, J.-T. Yang, Droplets coalescence and mixing with identical and distinct surface tension on a wettability gradient surface, Microfluid. Nanofluid., 14 (2013) 785-795.
[27] T.C. Sykes, D. Harbottle, Z. Khatir, H.M. Thompson, M.C.T. Wilson, Substrate Wettability Influences Internal Jet Formation and Mixing during Droplet Coalescence, Langmuir, 36 (2020) 9596-9607.
[28] G. Chen, B. Ji, Y. Gao, C. Wang, J. Wu, B. Zhou, W. Wen, Towards the rapid and efficient mixing on 'open-surface' droplet-based microfluidics via magnetic actuation, Sens. Actuators, B, 286 (2019) 181-190.
[29] S. Bansal, P. Sen, Mixing enhancement by degenerate modes in electrically actuated sessile droplets, Sens. Actuators, B, 232 (2016) 318-326.
[30] K.Y. Lee, S. Park, Y.R. Lee, S.K. Chung, Magnetic droplet microfluidic system incorporated with acoustic excitation for mixing enhancement, Sens. Actuators, A, 243 (2016) 59-65.
[31] A. Davanlou, R. Kumar, Passive mixing enhancement of microliter droplets in a thermocapillary environment, Microfluid. Nanofluid., 19 (2015) 1507-1513.
[32] H. Kinoshita, S. Kaneda, T. Fujii, M. Oshima, Three-dimensional measurement and visualization of internal flow of a moving droplet using confocal micro-PIV, Lab on a Chip, 7 (2007) 338-346.
[33] S. Zhao, W. Wang, M. Zhang, T. Shao, Y. Jin, Y. Cheng, Three-dimensional simulation of mixing performance inside droplets in micro-channels by Lattice Boltzmann method, Chem. Eng. J, 207-208 (2012) 267-277.
[34] C.Y. Pak, W. Li, Y.-L. Steve Tse, Free Energy and Dynamics of Water Droplet Coalescence, J. Phys. Chem. C, 122 (2018) 22975-22984.
[35] Q. Chen, C. Wang, X. Zhang, G. Chen, Q. Hu, H. Li, J. Wang, D. Wen, Y. Zhang, Y. Lu, G. Yang, C. Jiang, J. Wang, G. Dotti, Z. Gu, In situ sprayed bioresponsive immunotherapeutic gel for post-surgical cancer treatment, Nat. Nanotechnol., 14 (2019) 89-97.
[36] S. Plimpton, Fast Parallel Algorithms for Short-Range Molecular Dynamics, J. Comput. Phys.,117 (1995) 1-19.

[37] P.J. Hoogerbrugge, J.M.V.A. Koelman, Simulating Microscopic Hydrodynamic Phenomena with Dissipative Particle Dynamics Europhys. Lett., (1992) 155-160 .
[38] P.B. Warren, Vapor-liquid coexistence in many-body dissipative particle dynamics, Phys. Rev. E, 68 (2003) 066702.
[39] P Español, PB Warren, Perspective: Dissipative Particle Dynamics, 146(2016) 150901.
[40] Y. Xia, J. Goral, H. Huang, I. Miskovic, P. Meakin, M. Deo, Many-body dissipative particle dynamics modeling of fluid flow in fine-grained nanoporous shales, Phys. Fluids, 29 (2017) 056601.
[41] K. Zhang, Z. Li, M. Maxey, S. Chen, G.E. Karniadakis, Self-Cleaning of Hydrophobic Rough Surfaces by Coalescence-Induced Wetting Transition, Langmuir, 35 (2019) 2431-2442.
[42] C.-J. Wu, K.-C. Chu, Y.-J. Sheng, H.-K. Tsao, Sliding Dynamic Behavior of a Nanobubble on a Surface, Journal of Physical Chemistry C, 121 (2017) 17932-17940.
[43] P Español, PB Warren, Statistical Mechanics of Dissipative Particle Dynamics, Europhys. Lett., 30 (1995) 191-196.
[44] M. Arienti, W. Pan, X. Li, G. Karniadakis, Many-body dissipative particle dynamics simulation of liquid/vapor and liquid/solid interactions, J Chem Phys, 134 (2011) 204114.
[45] G. Yi, Z. Cai, Z. Gao, Z. Jiang, X. Huang, J.J. Derksen, Droplet impingement and wetting behavior on a chemically heterogeneous surface in the Beyond–Cassie–Baxter regime, AIChE Journal, 66 (2020) e16263.
[46] U.O.M. Vázquez, W. Shinoda, P.B. Moore, C.-c. Chiu, S.O. Nielsen, Calculating the surface tension between a flat solid and a liquid: a theoretical and computer simulation study of three topologically different methods, J. Math. Chem., 45 (2008) 161-174.
[47] M. Ahmadlouydarab, A.A. Hemeda, Y. Ma, Six Stages of Microdroplet Detachment from Microscale Fibers, Langmuir, 34 (2018) 198-204.
[48] X. Tong, J. Dong, Y. Shang, K. Inthavong, J. Tu, Effects of nasal drug delivery device and its orientation on sprayed particle deposition in a realistic human nasal cavity, Comput. Biol. Med., 77 (2016) 40-48.
[49] M.M. Farhangi, P.J. Graham, N.R. Choudhury, A. Dolatabadi, Induced Detachment of Coalescing Droplets on Superhydrophobic Surfaces, Langmuir, 28 (2012) 1290-1303
[50] R. Essajai, A. Mzerd, N. Hassanain, M. Qjani, Thermal conductivity enhancement of nanofluids composed of rod-shaped gold nanoparticles: Insights from molecular dynamics, J. Mol. Liq., 293 (2019) 111494.